

Embedding high loading and uniform Ni nanoparticles into silicalite-1 zeolite for dry reforming of methane

Yang Liu^{a,1}, Yong Chen^{a,1}, Zirui Gao^{b,1}, Xiao Zhang^a, Lejian Zhang^a, Meng Wang^b, Bingbing Chen^a, Yanan Diao^a, Yilong Li^a, Dequan Xiao^c, Xinping Wang^{a,*}, Ding Ma^{b,*}, Chuan Shi^{a,*}

^a State Key Laboratory of Fine Chemicals, School of Chemical Engineering, Dalian University of Technology, Dalian 116024, China

^b Beijing National Laboratory for Molecular Sciences, College of Chemistry and Molecular Engineering, and BIC-ESAT, Peking University, Beijing 100871, China

^c Center for Integrative Materials Discovery, Department of Chemistry and Chemical Engineering, University of New Haven, West Haven, CT 06516, USA



ARTICLE INFO

Keywords:

Embedded Ni NPs
Silicalite-1 zeolite
Dry reforming of methane

ABSTRACT

Embedding Ni nanoparticles (NPs) into supports has been widely accepted as one of solutions for Ni confinement, but high loading usually stands on the opposite of being well dispersed and encapsulated. Herein, we developed a controlled ‘dissolution-recrystallization’ method of embedding high loading and uniform Ni NPs into the shell of hollow silicalite-1 (S-1) zeolite. The sizes of Ni NPs maintained at ca. 4–5 nm with increasing Ni loading from 3% to 20%, and the TOF kept at ca. 60 s⁻¹ (800 °C) in the dry reforming of methane reaction. The augmented density of active sites with Ni loading rendered an outstanding reaction rate of 20.0 mol_{CH4}/g_{cat}/h over 20% Ni@S-1. The embedded structure also endowed a good stability upon running for 150 h. This study paves the way for embedding high loading and uniform metal nanoparticles inside the zeolite, providing an effective strategy to stabilize metals under harsh reaction conditions.

1. Introduction

Given that syngas is a key building block to produce a series of indispensable and value-added chemicals, as one of the most promising reaction to produce the syngas, dry reforming of methane (DRM, CH₄ + CO₂ → 2CO + 2H₂), has gained much attention in last decades, not only because of its conversion of greenhouse gases, but also the scientific significance of converting the two chemical stable molecules.

Though variety of metals (e.g. Rh, Pt, Pd Co, Fe and Ni) are reported as active components for DRM process [1–3], Ni-based catalysts are the most promising for industrialization due to their high activity but low cost. However, Ni-based catalysts suffer from metal sintering and coke deposition at high operating temperatures, leading to gradual catalyst deactivation. Significant efforts have been devoted to strengthening the metal support interaction and adding second-metal to anchor and stabilize Ni nanoparticles under harsh reaction conditions, or introducing promoters to adsorb/activate CO₂ to reduce carbon deposition [4–6]. Given all of these, encapsulating Ni nanoparticles (NPs) into supports has been of great interests because the restriction of Ni sintering could

be expected and the electronic structure of surface Ni species could be tuned via metal-support interaction which might be beneficial to reduce carbon deposition [7–9].

Silica substrate is one of superior candidates to embed Ni NPs due to its cheapness, well controlled synthesis and good thermal stability. Formation of nickel phyllosilicate intermediates during the synthesis represents the typical chemical strategies to stabilize Ni [10–12]. In addition, confinement of Ni NPs in composite structures like core-shell [13,14], yolk-shell [15,16] and sandwich [17,18] provides the physical strategy to hamper the particle growth as well. Thus combining the two strategies, nickel phyllosilicate intermediates in synthesis and confinement of Ni NPs in composite structures with a better shell could be a better attempt.

Featured by the regular channels and high thermal stability, silicalite-1 (S-1) zeolite has been a better candidate to confine Ni NPs [19–24]. As reported by Dai et al. [25], by using a ‘dissolution-recrystallization’ process over the as calcinated 1.5% NiO/S-1 sample, Ni NPs (ca. 3.4 nm) were encapsulated into the hollow nanobox of S-1 crystals and the catalyst performed a high initial CH₄

* Corresponding authors.

E-mail addresses: dlgwxp@dlut.edu.cn (X. Wang), dma@pku.edu.cn (D. Ma), chuanshi@dlut.edu.cn (C. Shi).

¹ These authors contributed equally.

conversion of 80%. Since the precursor for dissolution-recrystallization was NiO nanoparticles, which not soluable in the ‘dissolution-recrystallization’ process, they finally fell into the hollow boxes of S-1 crystals. Due to the poor interaction between NiO and S-1, NiO will grow into large particles when increasing the Ni loading. Recently, a serious peasecod-like Ni@S-2 was prepared via a one-pot hydrothermal route, and the optimal one with 0.3 wt% Ni NPs embedded only showed a 2.1% deactivation in 50 h at 650 °C due to the dual physical-chemical confinement [26]. Considering the DRM reaction, higher Ni loading is crucial to ensure a higher mass-specific reaction rate. While a Ni loading more than 5% [27] or 8% [28] would destroy S-1 zeolite structure in such one-pot synthesis route. Therefore, an embedded catalyst possessing high Ni dispersion in increasing loading remains great challenge for DRM reaction.

Herein, Ni^{2+} /S-1 instead of NiO/S-1 was used as precursor for ‘dissolution-recrystallization’ in a tetrapropylammonium hydroxide (TPAOH) solutions. Ni heteroatoms were incorporated into the S-1 lattice to form -Ni-O-Si- bonding during the recrystallization process, which linked NiO NPs with S-1 zeolite and made NiO nanoparticles embed into the shell of S-1 instead of being left in the cage of S-1 crystals upon calcination. Such unique synthesis strategy makes Ni NPs keeping high dispersion (4–5 nm) even at a Ni loading of 20 wt% after reduction, being great challenge for metal catalysts synthesis. The dual physical and chemical confinement structure with high density and uniform Ni NPs embedded into the shell of S-1 zeolite endows the reaction rate reaching as high as 20.0 mol $_{\text{CH}_4}/\text{g}_{\text{cat}}/\text{h}$ at 800 °C and a good stability for dry reforming of methane.

2. Experimental section

2.1. Catalyst preparation

Tetraethyl orthosilicate (TEOS), tetrapropylammonium hydroxide (TPAOH), nickel nitrate were sourced from Sinopharm Chemical Reagent Co., Ltd., ethanol was purchased from Macklin Company. All the chemicals were used without any purification.

Synthesis of S-1 zeolites: Parent S-1 crystals were prepared from the clear solution method [29]. 56.48 g of tetraethyl orthosilicate (TEOS), 58.32 g of tetrapropylammonium hydroxide (TPAOH) (25 wt%), 49.24 g of ethanol and 177.44 g of H₂O were mixed at room temperature with vigorously stirring. The mixture was stirred for 5 h and then heated in a teflon-lined stainless-steel autoclave at 170 °C for 3 days under autogenous pressure. The product was recovered by centrifugation and dried overnight at 100 °C. Finally, the template was removed by calcination in static air at 540 °C for 4 h, then the S-1 zeolite was obtained.

Synthesis of Ni@S-1 catalysts: The as-prepared S-1 zeolites were impregnated with aqueous solutions of Ni(NO₃)₂·6H₂O (2 mL of aqueous solution per gram of zeolite). The mixture was then stirred at room temperature until the complete evaporation of water. A series of samples with different metal loadings was obtained by using Ni(NO₃)₂·6H₂O solutions of various concentrations. Ni nanoparticles were encapsulated within S-1 crystals by treating the Ni impregnated crystals in TPAOH solutions (0.3 M, 40 mL of solution per gram of zeolite) at 170 °C for 3 days. After hydrothermal treatment, the as-synthesized samples (denoted as x% DR-Ni@S-1), where the x represents the metal loading determined by inductively coupled plasma mass spectrometry (ICP-MS), were collected by centrifugation and dried overnight at 100 °C. After removal of the organic template by calcining at 540 °C for 4 h, the samples with different Ni loadings were pretreated in hydrogen at 750 °C to obtain Ni@S-1. It is suggested that the up limit of Ni loading should be 20 wt%, since if the amount of Ni was further increased up to 25 wt%, it was shown in Fig. S1 that not all the Ni NPs were well confined into the zeolite and the matrix of S-1 zeolite was partially destroyed.

Synthesis of Ni/S-1 samples. Zeolites were impregnated with aqueous solutions of Ni(NO₃)₂·6H₂O by incipient-wetness impregnation

method with similar theoretical Ni loading to corresponding NiO@S-1 samples. The impregnated samples were dried overnight at 100 °C and then calcined at 540 °C for 4 h, denoted as NiO/S-1. Then the NiO/S-1 samples were pretreated in hydrogen at 600 °C to obtain Ni/S-1.

2.2. Catalyst characterization

X-ray powder diffraction (XRD) analysis was conducted using an XRD-6000 (Shimadzu, Kyoto, Japan) instrument with Cu K α radiation ($\lambda = 0.1542 \text{ nm}$), operating at 30 kV and 30 mA and at a scanning rate of 10 °/min. Diffraction peaks were recorded in a 2θ range of 20–90 °. Phase identification was achieved through the comparison of XRD patterns to those of the Joint Committee on Powder Diffraction Standards (JCPDS).

UV-vis spectrophotometer was conducted by using a UV-550 (190 nm – 900 nm) equipped with a diffuse reflectance accessory. The spectra were recorded in the range 200–500 nm at room temperature.

Field emission scanning electron microscope (SEM) was conducted on QUNATA200 FEG to observe morphology of the samples. All samples were sputtered with a thin film of gold.

Electron Microscopy (EM) analysis was conducted using Nion UltraSTEM-100 electron microscopy operated at 60 kV, FEI Titan Cubed Themis G2 operated at 300 kV and FEI F30 operated at 300 kV. The Z-contrast images were collected with an annular dark field detector in the range of 86–200 mrad with a convergence angle of 30 mrad on Nion. And Electron energy-loss spectroscopy was carried out with the same experimental set-up. While the Titan is equipped with an XFEG gun and Bruker Super-X EDS detectors, with a convergence semi-angle of 25 mrad, and a collection semi-angle snap in the range of 53–260 mrad. The samples for electron microscopy characterization were prepared by directly dropping in ethanol solvent on cubic grid coated holey carbon film.

Nitrogen adsorption-desorption was measured at –196 °C on Quanta chrome autosorbiQ2 gas adsorption analyzer, for which the samples were degassed at 300 °C under high vacuum for 6 h prior to the measurement. The Brunauer–Emmett–Teller (BET) method was applied to calculate the total surface area (S_{BET}), while the t-plot method was used to discriminate between micro- and meso-porosity. In the t-plot, the reported mesopore surface area (S_{meso}) consists of contributions from the outer surface of the particles as well as mesopores and macropores. The pore volumes and the average pore size of micropores and mesopores were calculated using the Barrett–Joyner–Halenda (BJH) model.

H₂ Temperature-programmed reduction (H₂-TPR) experiments were performed on a chemisorption analyzer (AutoChem II 2920), which equipped with a thermal conductivity detector (TCD). In detail, 100 mg as-prepared catalyst was pretreated in inert argon at 200 °C for 90 min with a 10 °C/min heating rate, and then cooled down to ambient temperature naturally. After switching to 10% H₂/Ar, the catalyst was heated to 800 °C at 10 °C/min and then held for 10 min.

H₂ pulse chemisorption was used to determine the amount of exposed Ni atoms on the above-mentioned chemisorption analyzer. 100 mg as-prepared samples were pretreated in 100 mL/min 50% H₂/Ar for 90 min at 750 °C (for Ni@S-1) or 600 °C (for Ni/S-1), and then switched to He and ramped to 770 °C or 620 °C to degas for 30 min and then cooled down to 0 °C. H₂ was dosed on the samples every 2.5 min until saturation.

Temperature-programmed oxidation (TPO) of spent catalysts. The catalysts after 50 h stability test were switched to exposed to 20% O₂/Ar (500 mL/min) at ambient temperature, after purging for 30 min, the fixed-bed reactor was heated to 800 °C at a rate of 10 °C/min and then held for 10 min. The CO and CO₂ were quantified by infrared absorption spectrometer (SICK-MAIHAK-S710, Germany), but CO₂ was the major product. The carbon deposition can be obtained from the following equation:

$$n_{\text{carbon deposition}} = \frac{\int c dt \times F}{22.4 \text{L/mol}}$$

$$\text{Normalized carbon deposition} = \frac{n_{\text{carbon deposition}}}{(n_{\text{converted CH}_4} + n_{\text{converted CO}_2}) \times n_{\text{Ni}}}.$$

where c was the concentration of CO_x , detected from the infrared absorption spectrometer; F was the flow rate of 20% O_2/Ar (500 mL/min).

2.3. Catalytic performance evaluations

The activity tests for dry reforming of methane of as-prepared catalysts were carried out in a continuous-flow, fixed-bed reactor. 60 mg of the catalyst (40–60 mesh) diluted with 240 mg of quartz sand (40–60 mesh) was loaded into the quartz tubular reactor. Prior to the tests, the fresh catalysts were reduced in pure hydrogen for 60 min at 750 °C (for Ni@S-1) or 600 °C (for Ni/S-1) to ensure a complete reduction of Ni^{2+} to Ni^0 (as proved by $\text{H}_2\text{-TPR}$ quantitative analysis shown in Fig. S2), and then cooled down or heated up to specified temperature in argon and switched to the feed of reactants ($\text{CH}_4/\text{CO}_2 = 1/1$) at a GHSV of 180,000 mL/g/h or 100,000 mL/g/h without any inert diluent gas. The effluent gases were analyzed by an online gas chromatograph (Tianmei 7900) equipped with a TDX-01 column connected to a thermal conductivity detector (TCD). The catalytic activity for each sample at an exact temperature were collected for every 15 min and it was unchanged after 30 min. The data were collected after running the reaction for 60 min. As for the stability test, we chose the samples with 15 wt% Ni content for its moderate loading to represent the properties of serious Ni@S-1 catalysts.

The CH_4 conversion, CO_2 conversion, reaction rate, TOF and carbon balance were calculated according to the listed equations:

$$X_{\text{CH}_4} (\%) = \frac{F_{\text{CH}_4,\text{in}} - F_{\text{CH}_4,\text{out}}}{F_{\text{CH}_4,\text{in}}} \times 100\%$$

$$X_{\text{CO}_2} (\%) = \frac{F_{\text{CO}_2,\text{in}} - F_{\text{CO}_2,\text{out}}}{F_{\text{CO}_2,\text{in}}} \times 100\%$$

$$\text{Reaction rate} = \frac{(F_{\text{CH}_4,\text{in}} - F_{\text{CH}_4,\text{out}})}{m_{\text{cat}} \times 22.4 \text{L/mol}}$$

$$\text{TOF} = \frac{\text{Reaction rate}}{\text{amount of Exposed Ni atoms}}$$

$$\text{Carbon balance (\%)} = \frac{F_{\text{CO}_2,\text{out}} + F_{\text{CO},\text{out}} + F_{\text{CH}_4,\text{out}}}{F_{\text{CO}_2,\text{in}} + F_{\text{CH}_4,\text{in}}} \times 100\%$$

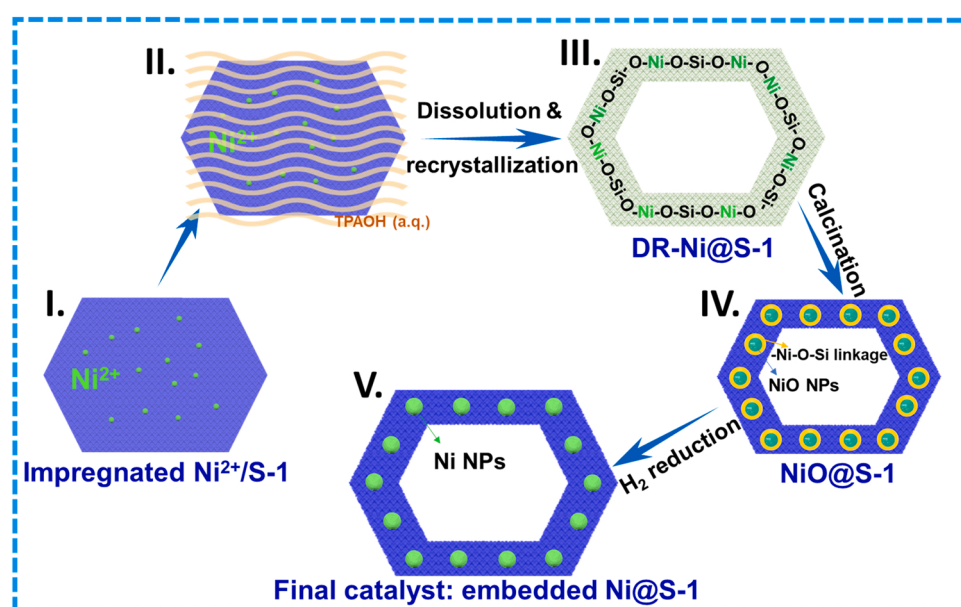
where $F_{\text{CH}_4,\text{in}}$, $F_{\text{CO}_2,\text{in}}$, $F_{\text{CH}_4,\text{out}}$ and $F_{\text{CO}_2,\text{out}}$ are the flow rates of CH_4 and CO_2 , in the feed or outlet. The carbon balance ranged between 98% and 102% for all the activity and stability test, and it was no longer showed elsewhere.

3. Results and discussion

3.1. Synthesis and characterizations

Synthesis of Ni nanoparticles embedded into S-1 zeolite was achieved by the controlled dissolution-recrystallization method as shown in Scheme 1. To be specific, the as-prepared S-1 zeolites were firstly impregnated by a designed amount of $\text{Ni}(\text{NO}_3)_2 \cdot 6\text{H}_2\text{O}$ solution (Step: I). After desiccation, the sample was dissolved and recrystallized in TPAOH solution (40 mL/gzeolite) under optimized conditions of 170 °C and 72 h without adding extra silicon source, and the obtained material was denoted as DR-Ni@S-1 (Step: II and III). After the calcination in air at 540 °C for 4 h, $\text{NiO}@S-1$ was obtained (Step: IV). Finally, the embedded Ni@S-1 was prepared upon reduction in H_2 at 750 °C (Step: V). Meanwhile, the reference samples with similar Ni content to Ni@S-1 samples were prepared by conventional impregnation method, which was denoted as Ni/S-1.

As indicated by XRD patterns of DR-Ni@S-1 samples (Fig. 1a), the diffraction peaks of S-1 zeolite shifted to lower angles after incorporation of Ni species, which is attributed to the enlarged cell volume of the zeolite by replacement of Si (0.111 Å) with Ni (0.124 Å) during the recrystallization. The incorporation of Ni into S-1 lattice was evidenced by UV-vis diffuse reflectance spectroscopy (Fig. 1b), the absorption peak at 218 nm was characteristic for the bond of $-\text{Ni}-\text{O}-\text{Si}-$ (the charge transfer transition of $\text{O}^{2-} \rightarrow \text{Ni}^{2+}$) [30,31]. As shown in Fig. 1c, the pre-edge of Ni K-edge XANES spectra of 15% DR-Ni@S-1 appeared at E^0 of 8333.9 eV, attributed to $1\text{s} \rightarrow 3\text{d}$ transition of Ni^{2+} , similar to that of NiO reference (8333.8 eV) [32]. Local coordination environment of the



Scheme 1. Schematic illustration of the steps for the synthesis of Ni@S-1 via ‘dissolution-recrystallization’ method. In brief, impregnated $\text{Ni}(\text{NO}_3)_2 \cdot 6\text{H}_2\text{O}$ (I) was dispersed in TPAOH-containing solution (II) to get DR-Ni@S-1 (III) through the following hydrothermal-treated process. Then, it was transformed into (IV) $\text{NiO}@S-1$ after calcination in air. Finally, the target catalyst, embedded Ni@S-1 (V), was obtained after H_2 treatment.

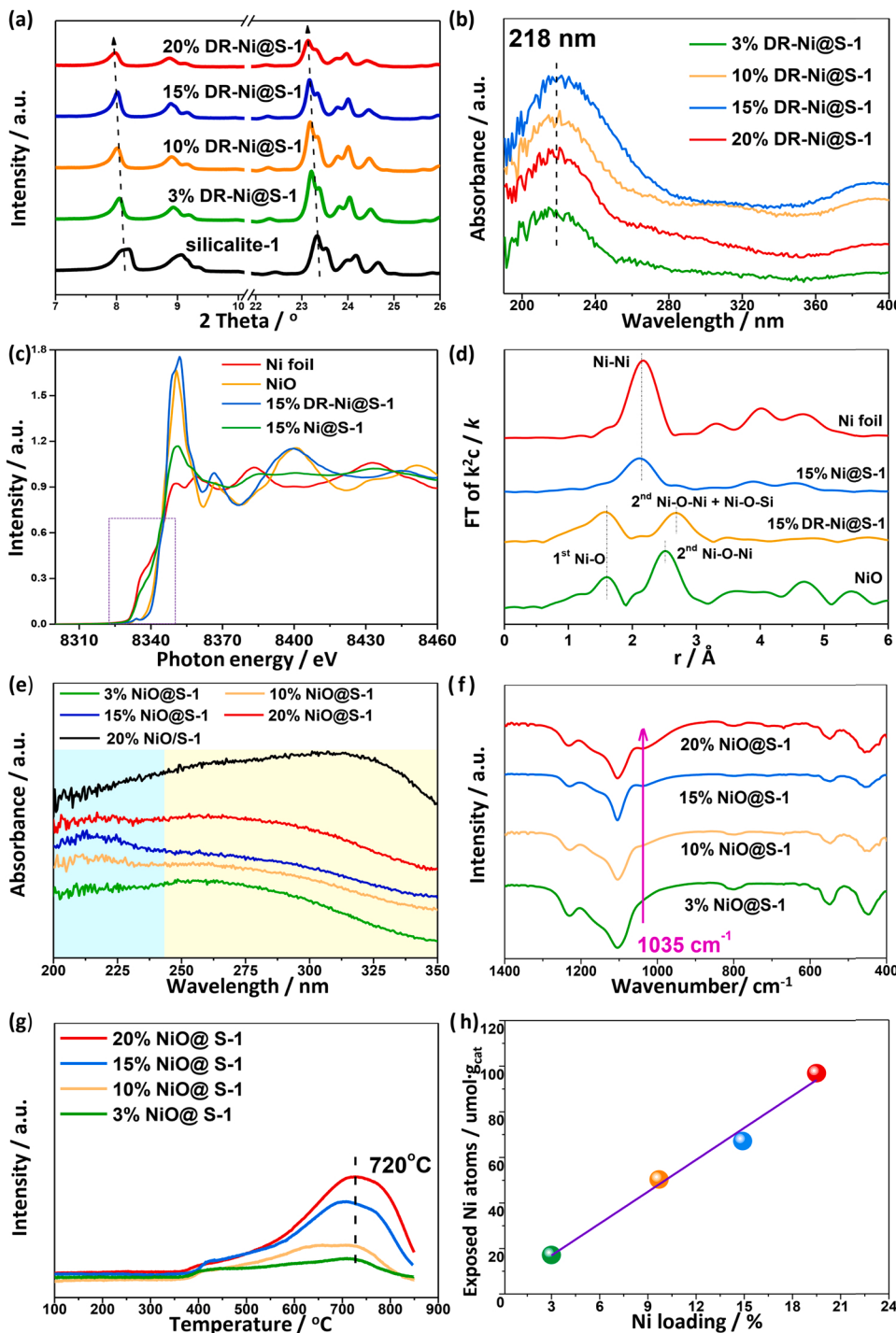


Fig. 1. Characterization of the samples during different synthesis stages. (a) XRD patterns of the DR-Ni@S-1 samples with different Ni loadings; (b) UV-vis of the DR-Ni@S-1 samples with different Ni loadings; (c) Normalized Ni K-edge XANES spectra for 15% DR-Ni@S-1 and 15% Ni@S-1; Ni foil and NiO were used as references; (d) Fourier transform Ni K-edge EXAFS spectra for 15% DR-Ni@S-1 and 15% Ni@S-1; Ni foil and NiO were used as references; (e) UV-vis of the NiO@S-1 samples with different Ni loadings and the 20% NiO/S-1 reference; (f) FTIR spectra of NiO@S-1 and NiO/S-1 samples with different Ni loadings; (g) H₂-TPR profiles of the NiO@S-1 samples with different Ni loadings; (h) Exposed Ni atoms detected by H₂ pulse chemisorption of the Ni@S-1 samples with different Ni loadings.

Ni species analyzed by FT EXAFS of Ni K-edge (Fig. 1d, S3 and Tab. S1) showed a peak at 1.6 Å, similar to NiO reference in the first coordination shell, indicating that Ni neighbored with O atoms to form Ni-O bonds with a length of 2.09 Å. But the r value obviously shifted at the second coordination shell from 2.5 Å to 2.7 Å, indicating the replacement of Ni by Si atoms and consequent formation of –Ni–O–Si– bonds, and the bond length was enlarged from 2.98 Å to 3.01 Å concurrently [26]. Such newly-formed –Ni–O–Si– species during the controlled dissolution-recrystallization process bonded NiO NPs with S-1 zeolite upon calcination as shown in the following section.

After calcination in air, the diffraction peaks of NiO were not observed over the series of NiO@S-1 samples in XRD patterns (Fig. S4),

indicating the high dispersion of NiO nanoparticles. In comparison, the diffraction peaks of NiO (yellow shadow) were detected over all the four NiO/S-1 samples (Fig. S5), and the peak intensity enhanced with the increasing Ni loading, indicating a weak interaction between NiO with S-1 zeolite over the impregnated NiO/S-1 samples. As for UV-vis spectra of NiO@S-1 (Fig. 1e), the broad bands spanning from 250 to 320 nm (buff shadow) dominated, which belonged to the O²⁻ (2p) → Ni²⁺ (3d) charge transfer of octahedral Ni²⁺ in NiO clusters [33]. In comparison, the band of 20% NiO/S-1 was at higher wavelength, reflecting its larger NiO particle size [4,31]. Besides that, the absorption peak at 218 nm corresponding to –Ni–O–Si– species were still visible over the calcinated NiO@S-1 samples. It was also detected by FTIR as shown in Fig. 1 f, a

band at 1035 cm^{-1} ascribed to asymmetrical stretching vibration of the $-\text{Ni}-\text{O}-\text{Si}-$ appeared over all the NiO/S-1 samples [34,35], and the intensity increased with Ni content. On this basis, a composite ‘core-linkage-shell’ structure was proposed that $-\text{Ni}-\text{O}-\text{Si}-$ species linked the NiO core and S-1 shell. Such structure well explained the H_2 -temperature programmed reduction ($\text{H}_2\text{-TPR}$) behaviors of all the NiO/S-1 samples shown in Fig. 1 g. As temperature rose, the broad peaks ranging from 430 to $800\text{ }^\circ\text{C}$, were attributed to the reduction of the $-\text{Ni}-\text{O}-\text{Si}-$ linkage and consequent NiO NPs in the core (peaked at ca.

$720\text{ }^\circ\text{C}$) [27,36–38]. In comparison, such a linkage cannot be detected over the NiO/S-1 samples, and the NiO particles were reduced at $415\text{ }^\circ\text{C}$ (Fig. S6), verifying the weak interaction between NiO with S-1 zeolite over the impregnated NiO/S-1 samples again. Such discrepancy between NiO/S-1 and NiO/S-1 samples clearly interpreted the superiority of NiO/S-1 samples synthesized via the ‘dissolution-recrystallization’ method [39].

After reduction of NiO/S-1 by H_2 at $750\text{ }^\circ\text{C}$ (designated as Ni@S-1), no metallic Ni phase or other Ni species were detected by XRD (Fig. S7).

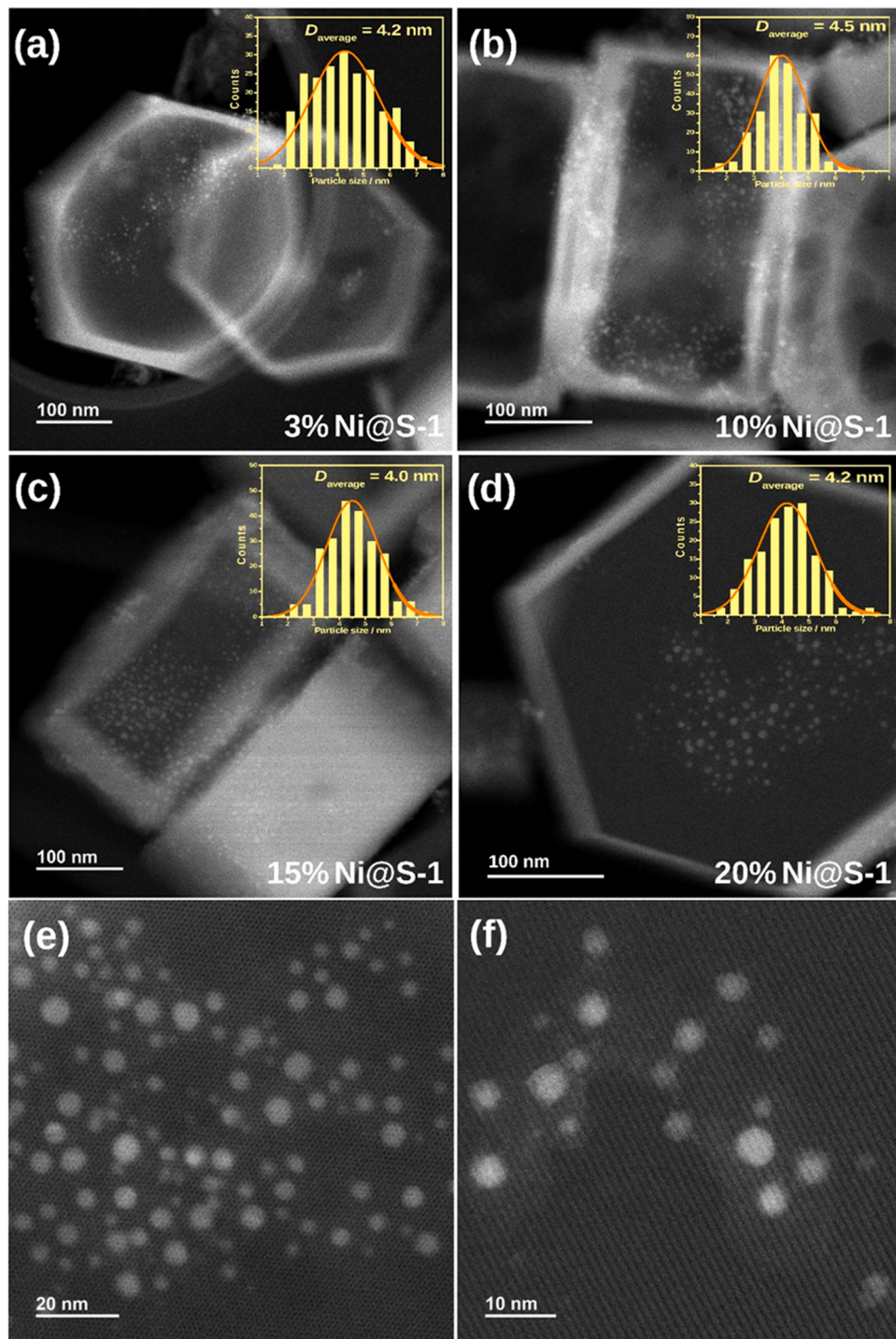


Fig. 2. Scanning transmission electron microscopy characterization for the Ni@S-1 catalysts. (a-d) STEM-HAADF (high-angle annular dark-field) images of the Ni@S-1 catalysts with different Ni loadings; The insets show the corresponding Ni NPs size distributions; High magnification STEM-HAADF image of 15% Ni@S-1 on frontal view (e) and side view (f);

According to EXAFS, Ni K-edge XANES (Fig. 1d-e), and the quasi-in-situ XPS results (Fig. S8), the Ni species in Ni@S-1 were reduced to Ni^0 . H_2 pulse chemisorption results (Fig. 1 h), representing the amounts of exposed Ni atoms [40], indicated that the amount of exposed Ni atoms grew linearly with increase of Ni loading, suggesting that Ni NPs did not aggregate into larger particles and decrease their dispersions upon

enhancing Ni loadings up to 20 wt%. Moreover, scanning transmission electron microscopy (STEM) images of the series of Ni@S-1 with different Ni loadings (Fig. 2a-d and S9) exhibited that the size of Ni nanoparticles maintained at ca. 4–5 nm when Ni loading increased from 3% to 20%. This, on the other hand, confirmed the embedded structure of this Ni@S-1 catalysts, being contrary with those Ni NPs dispersed on

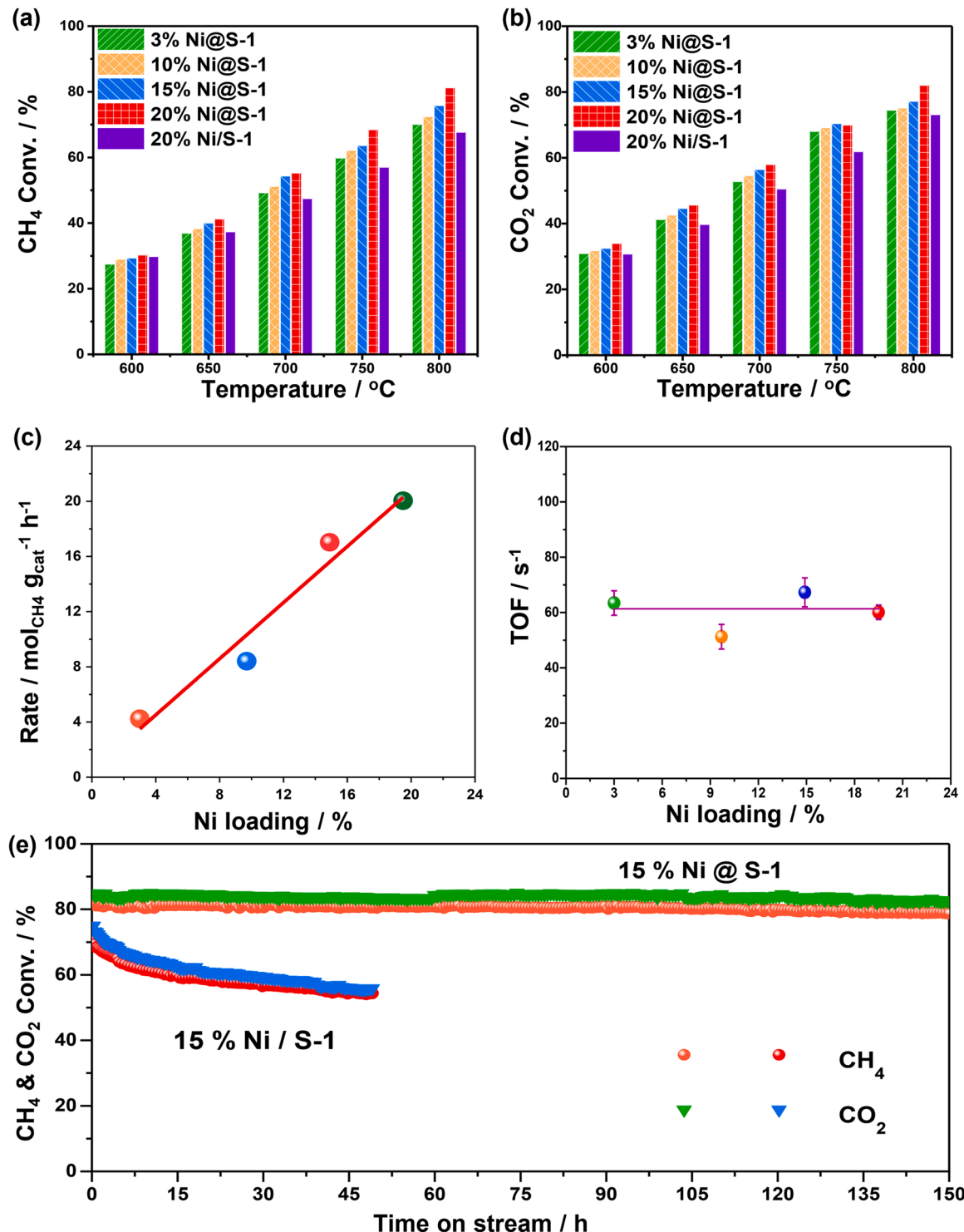


Fig. 3. Catalytic Performance of Ni@S-1 catalysts in DRM reaction. Dependence of CH_4 conversion (a) and CO_2 conversion (b) on reaction temperature over the Ni@S-1 catalysts with different Ni loadings and the referential 20% Ni/S-1 catalysts. ($\text{CO}_2:\text{CH}_4 = 1:1$, WHSV=180,000 mL/g/h); (c) Dependence of CH_4 reaction rates (under kinetic conditions) on Ni loading over Ni@S-1 catalysts. ($T = 800^\circ\text{C}$, $\text{CO}_2:\text{CH}_4 = 1:1$). (d) Dependence of TOFs on Ni loadings over Ni@S-1 catalysts. ($T = 800^\circ\text{C}$, $\text{CO}_2:\text{CH}_4 = 1:1$). (e) CH_4 and CO_2 conversion of 15% Ni@S-1 and 15% Ni/S-1 catalysts versus time on stream at 800°C ($\text{CO}_2:\text{CH}_4 = 1:1$, WHSV=100,000 mL/g/h).

the outer surface of the support that may aggregate into larger particles samples with increasing Ni loading (Fig. S10). To be more specific, in the high magnification STEM-HAADF images (Fig. 2e-f), the zeolite channel structure was intact passing through the Ni NPs on both frontal and side view, clearly indicating the embedded structure.

The textural properties were characterized and summarized in Figure. S9 and Tab. S2. As can be seen, the BET surface area of 15% Ni@S-1 was $427 \text{ m}^2/\text{g}$, slightly lower than that of S-1 zeolite ($477 \text{ m}^2/\text{g}$). Moreover, after incorporation of Ni species into S-1, micropore area and micropore volume decreased from $425 \text{ m}^2/\text{g}$ and $0.185 \text{ cm}^3/\text{g}$ to $230 \text{ m}^2/\text{g}$ and $0.106 \text{ cm}^3/\text{g}$, respectively. This may be a profound effect of the dissolution-recrystallization process, during which some of micropores might be collapsed and transformed into mesopores [27]. Meanwhile, external surface area increased obviously due to the dealumination during thermal treatment [41]. These results coincide well with the observation from pore size distributions and N_2 adsorption/desorption isotherms. As can be seen, the bimodal-distributed pore size distribution at $0\text{--}1.1 \text{ nm}$ and $1.2\text{--}8.0 \text{ nm}$ was maintained after introducing Ni, but mesopores were enlarged (Fig. S11b). And the appearance of hysteresis loop in Fig. S11a pointed to a same conclusion. The enlarged micropores and mesopores might reduce the steric hindrance and facilitate the mass transfer of the reactants and products molecules [42–44].

3.2. Catalytic performance of Ni@S-1 catalysts

The catalytic performance of Ni@S-1 and the referential Ni/S-1 samples in DRM reaction was shown in Fig. 3a and Fig. 3b, respectively. Before reaction, the catalysts were pre-reduced in hydrogen at 750°C and 600°C (according to H₂-TPR results), respectively. The CH₄ and CO₂ conversions increased with Ni loading and reached 81.2% and 82.0% respectively over 20% Ni@S-1 sample at 800°C and WHSV of 180,000 mL/g/h (WHSV is high enough to keep the conversions away from the equilibrium). The mass-specific reaction rates at 800°C measured under kinetic conditions [45] showed linearly dependence on nickel loadings, as depicted in Fig. 3c. The rate can reach $20.0 \text{ mol}_{\text{CH}_4}/\text{g}_{\text{cat}}/\text{h}$ at 800°C over 20% Ni@S-1, about 1.8 times of the referential 20% Ni/S-1 (Fig. S12), representing one of the most active catalysts for the DRM reaction compared to those in the literatures (Tab. S3). Moreover, as illustrated in Fig. 3d, the turnover frequency (TOF) of CH₄ conversion over all the catalysts at 800°C are similar, at ca. 60 s^{-1} , almost unchanged with Ni loading. The results indicated that the increase of Ni content did not change the essence and status of nickel but only augmented the number of active sites, due to its unique embedded structure. The H₂/CO ratios over Ni@S-1 were lower than 1 due to the side reaction of reverse water gas shift [46], as shown in Fig. S13a. And the ratios increased with the reaction temperatures because DRM is

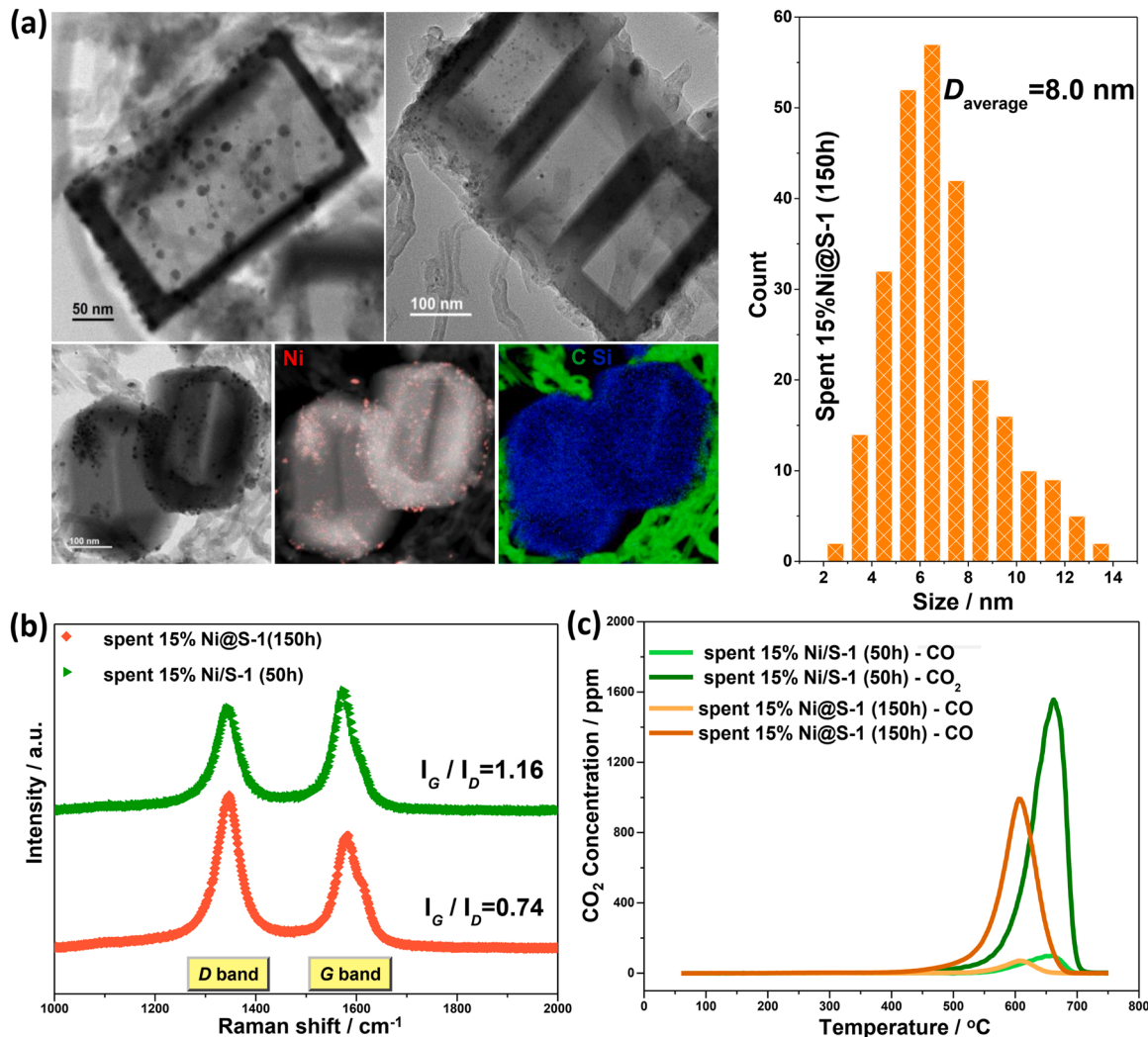


Fig. 4. Characterizations of the spent catalysts. (a) Left: STEM images with EELS elements maps of Ni (red), C (green) and Si (blue); Right corresponding Ni nanoparticles sizes distribution of the spent 15%Ni@S-1 (150 h); (b) Raman spectra of the spent 15% Ni@S-1 and 15% Ni/S-1 catalysts. (c) TPO profiles of the spent 15% Ni@S-1 and 15% Ni/S-1 catalysts.

thermodynamically favorable at high operating temperatures (Fig. S13b). Furthermore, the CH₄ and CO₂ conversions over 15% Ni@S-1 catalyst was almost unchanged under WHSV of 100, 000 mL/g/h at 800 °C in 150 h (Fig. 3e) and at 600 °C in 150 h (Fig. S14). However, the 15% Ni/S-1 catalyst suffered from deactivation apparently under the same space velocity at 800 °C. Such great discrepancy in activity and stability between the embedded Ni@S-1 and impregnated Ni/S-1 catalysts suggest that the embedded structure of Ni@S-1 not only keeps Ni NPs in high dispersion to possess a higher TOF, but also confines Ni NPs into the S-1 matrix to endow an excellent stability.

3.3. Characterizations of the spent catalysts

For the spent 15% Ni@S-1 catalyst (after running at above 800 °C for 150 h), nickel nanoparticles were still well dispersed (Fig. 4a), but the average size increased to ca. 8 nm. This may be attributed to slight breakage of the zeolites. In sharp contrast, the impregnated 15% Ni/S-1 sample suffered severely from sintering, the average size of nickel particles dramatically grew to ca. 26 nm in 8 h (Fig. S15). Such discrepancy gave clear evidence that Ni nanoparticles being confined into the matrix of S-1 zeolite possessed better resistance of sintering and thus better catalytic stability.

The deposited carbon on the spent catalysts were detected in XRD (Fig. S16), STEM images (Fig. 4a and S17), and Raman spectra (Fig. 4b). The lower IG/ID ratio of the 15% Ni@S-1 catalyst than that of 15% Ni/S-1 indicated the less graphitic degree of the deposit carbon and the coke might easier to be eliminated [47,48]. This was consistent with O₂-TPO results of the spent catalysts (Fig. 4c). Compared with Ni/S-1, the Ni@S-1 catalyst performed a larger low-temperature oxidation peak and the whole oxidation region shifted to lower temperature [49], suggesting the deposited carbon over Ni@S-1 was easier to be oxidized and removed. The normalized amounts of coke were 3.3 and 23.6 mmol carbon/mol converted CH₄ and CO₂/mol_{Ni} over 15% Ni@S-1 and 15% Ni/S-1, respectively, being consistent with its better coke resistance and catalytic stability of Ni@S-1 catalyst. And the coke inhibition capability of 15% Ni@S-1 was also better than majority of reported similar catalysts, as shown in Tab. S4. In addition, the carbon deposition on spent 15% Ni@S-1 was located out of the crystal rather than covering on Ni nanoparticles according to the EELS (electron energy loss spectroscopy) elemental maps in Fig. 4a., which was consistent with little side-effect on the catalytic performance.

4. Conclusions

A controlled strategy of ‘dissolution-recrystallization’ process to embed high density and uniform Ni NPs into the shell of hollow silicalite-1 zeolite was designed. Ni heteroatoms were incorporated into the lattice S-1 zeolite to form -Ni-O-Si- bond during the ‘dissolution-recrystallization’ process. Such chemical bonding induced strong interactions between NiO clusters and S-1 upon calcination, leading to the formation of uniform Ni NPs embedded into the shells of hollow S-1 after reduction. Due to the unique embedded structure, the series of Ni@S-1 samples showed similar TOFs of ca. 60 s⁻¹ in DRM and 20% Ni@S-1 performed a mass specific rate of 20.0 mol_{CH₄}/g_{cat}/h at 800 °C. Moreover, the embedded structure endowed Ni@S-1 to exhibit stable CH₄ and CO₂ conversions during the tested hours at 800 °C. This work highlights new opportunities to confine high density of active metal NPs in zeolite, being crucial to achieve high reaction rate and stability under harsh reaction conditions.

CRediT authorship contribution statement

Yang Liu: Investigation, Methodology, Data curation, Writing – original draft; Writing – review & editing, Visualization. **Yong Chen:** Methodology, Data curation, Writing – review & editing. **Zirui Gao:**

Methodology, Data curation, Writing – original draft, Writing – review & editing, Investigation. **Xiao Zhang:** Data curation, Writing – review & editing, Methodology. **Lejian Zhang:** Methodology, Data curation. **Meng Wang:** Data curation, Writing – review & editing, Methodology. **Bingbing Chen:** Data curation, Writing – review & editing. **Yanan Diao:** Data curation, Writing – review & editing. **Yilong Li:** Data curation. **Dequan Xiao:** Writing – review & editing. **Xingping Wang:** Writing – review & editing, Supervision. **Ding Ma:** Writing – review & editing, Funding acquisition, Supervision, Project administration. **Chuan Shi:** Writing – review & editing, Funding acquisition, Supervision, Project administration.

Declaration of Competing Interest

The authors declare that they have no known competing financial interests or personal relationships that could have appeared to influence the work reported in this paper.

Acknowledgement

The work was supported by the National Natural Science Foundation of China (Nos. 21872014, 21932002, 21902018 and 22076017), the National Key R&D Program of China (No. 2017YFA0700103 and 2021YFA1501100), the Fundamental Research Funds for the Central Universities (DUT20ZD205) and the Natural Science Foundation of Liaoning Province (2019-MS-053).

Appendix A. Supporting information

Supplementary data associated with this article can be found in the online version at doi:10.1016/j.apcatb.2022.121202.

References

- [1] Z. Li, Q. Lin, M. Li, J. Cao, F. Liu, H. Pan, Z. Wang, S. Kawi, Recent advances in process and catalyst for CO₂ reforming of methane, Renew. Sustain. Energy Rev. 134 (2020) 110312–112754.
- [2] Z. Liu, D.C. Grinter, P.G. Lustemberg, T.-D. Nguyen-Phan, Y. Zhou, S. Luo, I. Waluyo, E.J. Crumlin, D.J. Stacchiola, J. Zhou, J. Carrasco, H.F. Busnengo, M.V. Ganduglia-Pirovano, S.D. Senanayake, J.A. Rodriguez, Dry Reforming of Methane on a Highly-Active Ni-CeO₂ Catalyst: Effects of Metal-Support Interactions on C–H Bond Breaking, Angew. Chem. Int. Ed. 55 (2016) 7455–7459.
- [3] N. Köpfle, T. Götsch, M. Grünbacher, E.A. Carbonio, M. Hävecker, A. Knop-Gericke, L. Schlicker, A. Doran, D. Kober, A. Gurlo, S. Penner, B. Klötzer, Zirconium-Assisted Activation of Palladium To Boost Syngas Production by Methane Dry Reforming, Angew. Chem. Int. Ed. 57 (2018) 14613–14618.
- [4] Z. Li, M. Li, Z. Bian, Y. Kathiraser, S. Kawi, Design of highly stable and selective core/yolk-shell nanocatalysts—A review, Appl. Catal. B: Environ. 188 (2016) 324–341.
- [5] Y. Tang, Y. Wei, Z. Wang, S. Zhang, Y. Li, L. Nguyen, Y. Li, Y. Zhou, W. Shen, F. F. Tao, P. Hu, Synergy of Single-Atom Ni₁ and Ru₁ Sites on CeO₂ for Dry Reforming of CH₄, J. Am. Chem. Soc. 141 (2019) 7283–7293.
- [6] S. Das, A. Jangam, S. Jayaprakash, S. Xi, K. Hidajat, K. Tomishige, S. Kawi, Role of lattice oxygen in methane activation on Ni-phyllosilicate@Ce1-xZrxO₂ core-shell catalyst for methane dry reforming: Zr doping effect, mechanism, and kinetic study, Appl. Catal. B: Environ. 290 (2021), 119998.
- [7] Z. Li, Z. Wang, B. Jiang, S. Kawi, Sintering resistant Ni nanoparticles exclusively confined within SiO₂ nanotubes for CH₄ dry reforming, Catal. Sci. Technol. 8 (13) (2018) 3363–3371.
- [8] Z. Li, S. Kawi, Multi-Ni@Ni phyllosilicate hollow sphere for CO₂ reforming of CH₄: influence of Ni precursors on structure, sintering, and carbon resistance, Catal. Sci. Technol. 8 (7) (2018) 1915–1922.
- [9] Z. Li, Z. Wang, S. Kawi, Sintering and Coke Resistant Core/Yolk Shell Catalyst for Hydrocarbon Reforming, ChemCatChem 11 (1) (2019) 202–224.
- [10] Z. Li, B. Jiang, Z. Wang, S. Kawi, High carbon resistant Ni@Ni phyllosilicate@SiO₂ core shell hollow sphere catalysts for low temperature CH₄ dry reforming, J. CO₂ Util. 27 (2018) 238–246.
- [11] Z. Bian, I.Y. Suryawinata, S. Kawi, Highly carbon resistant multicore-shell catalyst derived from Ni-Mg phyllosilicate nanotubes@silica for dry reforming of methane, Appl. Catal. B: Environ. 195 (2016) 1–8.
- [12] Z. Bian, S. Kawi, Highly carbon-resistant Ni-Co/SiO₂ catalysts derived from phyllosilicates for dry reforming of methane, J. CO₂ Util. 18 (2017) 345–352.
- [13] F. Wang, B. Han, L. Zhang, L. Xu, H. Yu, W. Shi, CO₂ reforming with methane over small-sized Ni@SiO₂ catalysts with unique features of sintering-free and low carbon, Appl. Catal. B: Environ. 235 (2018) 26–35.

- [14] S. Das, J. Pérez-Ramírez, J. Gong, N. Dewangan, K. Hidajat, B.C. Gates, S. Kawi, Core-shell structured catalysts for thermocatalytic, photocatalytic, and electrocatalytic conversion of CO₂, Chem. Soc. Rev. 49 (10) (2020) 2937–3004.
- [15] Y. Lu, D. Guo, Y. Zhao, P.S. Moyo, Y. Zhao, S. Wang, X. Ma, Enhanced catalytic performance of Ni_x-V@HSS catalysts for the DRM reaction: The study of interfacial effects on Ni-Vox structure with a unique yolk-shell structure, J. Catal. 396 (2021) 65–80.
- [16] Z. Li, Y. Kathiraser, S. Kawi, Facile Synthesis of High Surface Area Yolk–Shell Ni@Ni Embedded SiO₂ via Ni Phyllosilicate with Enhanced Performance for CO₂ Reforming of CH₄, ChemCatChem 7 (2015) 160–168.
- [17] Z. Bian, S. Kawi, Sandwich-Like Silica@Ni@Silica Multicore–Shell Catalyst for the Low-Temperature Dry Reforming of Methane: Confinement Effect Against Carbon Formation, ChemCatChem 10 (1) (2018) 320–328.
- [18] S. Das, J. Ashok, Z. Bian, N. Dewangan, M.H. Wai, Y. Du, A. Borgna, K. Hidajat, S. Kawi, Silica–Ceria sandwiched Ni core-shell catalyst for low temperature dry reforming of biogas: Coke resistance and mechanistic insights, Appl. Catal. B: Environ. 230 (2018) 220–236.
- [19] W. Wang, W. Zhou, W. Li, X. Xiong, Y. Wang, K. Cheng, J. Kang, Q. Zhang, Y. Wang, In-situ confinement of ultrasmall palladium nanoparticles in silicalite-1 for methane combustion with excellent activity and hydrothermal stability, Appl. Catal. B: Environ. 276 (2020), 119142.
- [20] Y. Wang, Z.-P. Hu, X. Lv, L. Chen, Z.-Y. Yuan, Ultrasmall PtZn bimetallic nanoclusters encapsulated in silicalite-1 zeolite with superior performance for propane dehydrogenation, J. Catal. 385 (2020) 61–69.
- [21] Z. Li, S. Das, P. Hongmanrom, N. Dewangan, M.H. Wai, S. Kawi, Silica-based micro- and mesoporous catalysts for dry reforming of methane, Catal. Sci. Technol. 8 (11) (2018) 2763–2778.
- [22] J. Gu, Z. Zhang, P. Hu, L. Ding, N. Xue, L. Peng, X. Guo, M. Lin, W. Ding, Platinum Nanoparticles Encapsulated in MFI Zeolite Crystals by a Two-Step Dry Gel Conversion Method as a Highly Selective Hydrogenation Catalyst, ACS Catal. 5 (2015) 6893–6901.
- [23] N. Wang, Q. Sun, R. Bai, X. Li, G. Guo, J. Yu, In Situ Confinement of Ultrasmall Pd Clusters within Nanosized Silicalite-1 Zeolite for Highly Efficient Catalysis of Hydrogen Generation, J. Am. Chem. Soc. 138 (2016) 7484–7487.
- [24] H. Wang, L. Wang, F.-S. Xiao, Metal@Zeolite Hybrid Materials for Catalysis, ACS Cent. Sci. 6 (2020) 1685–1697.
- [25] C. Dai, S. Zhang, A. Zhang, C. Song, C. Shi, X. Guo, Hollow zeolite encapsulated Ni–Pb bimetallics for sintering and coking resistant dry reforming of methane, J. Mater. Chem. A 3 (2015) 16461–16468.
- [26] J. Wang, Y. Fu, W. Kong, F. Jin, J. Bai, J. Zhang, Y. Sun, Design of a carbon-resistant Ni@S-2 reforming catalyst: Controllable Ni nanoparticles sandwiched in a peacock-like structure, Appl. Catal. B: Environ. 282 (2021), 119546.
- [27] G. Vitale, H. Molero, E. Hernandez, S. Aquino, V. Birss, P. Pereira-Almao, One-pot preparation and characterization of bifunctional Ni-containing ZSM-5 catalysts, Appl. Catal. A: Gen. 452 (2013) 75–87.
- [28] X. Li, B. Li, J. Xu, Synthesis and characterization of transitional metal-rich zeolite M-MFI (M=Fe, Co, Ni, Cu) with regular mesoporous channels, Colloids Surf. A: Physicochem. Eng. Asp. 434 (2013) 287–295.
- [29] C. Dai, A. Zhang, L. Li, K. Hou, F. Ding, J. Li, D. Mu, C. Song, M. Liu, X. Guo, Synthesis of Hollow Nanocubes and Macroporous Monoliths of Silicalite-1 by Alkaline Treatment, Chem. Mater. 25 (2013) 4197–4205.
- [30] G. Garbarino, S. Chitsazan, T.K. Phung, P. Riani, G. Busca, Preparation of supported catalysts: A study of the effect of small amounts of silica on Ni/Al₂O₃ catalysts, Appl. Catal. A: Gen. 505 (2015) 86–97.
- [31] B. Lu, Y. Ju, T. Abe, K. Kawamoto, Grafting Ni particles onto SBA-15, and their enhanced performance for CO₂ methanation, RSC Adv. 5 (2015) 56444–56454.
- [32] L. Lin, Q. Yu, M. Peng, A. Li, S. Yao, S. Tian, X. Liu, A. Li, Z. Jiang, R. Gao, X. Han, Y.-w. Li, X.-d. Wen, W. Zhou, D. Ma, Atomically Dispersed Ni/o-MoC Catalyst for Hydrogen Production from Methanol/Water, J. Am. Chem. Soc. 143 (2021) 309–317.
- [33] S. Hu, W.-X. Li, Sabatier principle of metal-support interaction for design of ultrastable metal nanocatalysts, Science 374 (6573) (2021) 1360–1365.
- [34] S.C. Laha, P. Mukherjee, S.R. Sainkar, R. Kumar, Cerium Containing MCM-41-Type Mesoporous Materials and their Acidic and Redox Catalytic Properties, J. Catal. 207 (2002) 213–223.
- [35] S. Kongwudthiti, P. Praserthdam, W. Tanakulrungsank, M. Inoue, The influence of Si–O–Zr bonds on the crystal-growth inhibition of zirconia prepared by the glycothermal method, J. Mater. Process. Technol. 136 (2003) 186–189.
- [36] C. Zhang, H. Yue, Z. Huang, S. Li, G. Wu, X. Ma, J. Gong, Hydrogen Production via Steam Reforming of Ethanol on Phyllosilicate-Derived Ni/SiO₂: Enhanced Metal-Support Interaction and Catalytic Stability, ACS Sustain. Chem. Eng. 1 (2013) 161–173.
- [37] A.J. Maia, B. Louis, Y.L. Lam, M.M. Pereira, Ni-ZSM-5 catalysts: Detailed characterization of metal sites for proper catalyst design, J. Catal. 269 (2010) 103–109.
- [38] H. Peng, X. Zhang, L. Zhang, C. Rao, J. Lian, W. Liu, J. Ying, G. Zhang, Z. Wang, N. Zhang, X. Wang, One-Pot Facile Fabrication of Multiple Nickel Nanoparticles Confined in Microporous Silica Giving a Multiple-Cores@Shell Structure as a Highly Efficient Catalyst for Methane Dry Reforming, ChemCatChem 9 (2017) 127–136.
- [39] F. Yang, S. Zhou, S. Gao, X. Liu, S. Long, Y. Kong, In situ embedding of ultra-fine nickel oxide nanoparticles in HMS with enhanced catalytic activities of styrene epoxidation, Microporous Mesoporous Mater. 238 (2017) 69–77.
- [40] J. Zhang, F. Li, Coke-resistant Ni@SiO₂ catalyst for dry reforming of methane, Applied Catalysis B: Environmental 176–177 (2015) 513–521.
- [41] F. Goodarzi, L. Kang, F.R. Wang, F. Joensen, S. Kegnaas, J. Mielby, Methanation of Carbon Dioxide over Zeolite-Encapsulated Nickel Nanoparticles, ChemCatChem 10 (2018) 1566–1570.
- [42] N. Masoumifard, R. Guillet-Nicolas, F. Kleitz, Synthesis of Engineered Zeolitic Materials: From Classical Zeolites Hierarchical Core–Shell Materials, Adv. Mater. 30 (2018), 1704439.
- [43] S. van Donk, A.H. Janssen, J.H. Bitter, K.P. de Jonghs, Generation, Characterization, and Impact of Mesopores in Zeolite Catalysts, Catal. Rev. 45 (2003) 297–319.
- [44] A.R. Morgado Prates, C. Daniel, C. Pagis, Y. Schuurman, A. Tuvel, D. Farrusseng, Faster transport in hollow zeolites, Microporous Mesoporous Mater. 308 (2020), 110499.
- [45] M. Zhang, M. Wang, B. Xu, D. Ma, How to Measure the Reaction Performance of Heterogeneous Catalytic Reactions Reliably, Joule 3 (2019) 2876–2883.
- [46] J. Niu, Y. Wang, S.E. Liland, S.K. Regli, J. Yang, K.R. Rout, J. Luo, M. Rønning, J. Ran, D. Chen, Unraveling Enhanced Activity, Selectivity, and Coke Resistance of Pt–Ni Bimetallic Clusters in Dry Reforming, ACS Catal. 11 (2021) 2398–2411.
- [47] K. Cao, M. Gong, J. Yang, J. Cai, S. Chu, Z. Chen, B. Shan, R. Chen, Nickel catalyst with atomically-thin meshed cobalt coating for improved durability in dry reforming of methane, J. Catal. 373 (2019) 351–360.
- [48] X. Zhao, H. Li, J. Zhang, L. Shi, D. Zhang, Design and synthesis of NiCe@m-SiO₂ yolk-shell framework catalysts with improved coke- and sintering-resistance in dry reforming of methane, Int. J. Hydron. Energy 41 (2016) 2447–2456.
- [49] Y. Yang, Y.-K. Li, Y.-X. Zhao, G.-P. Wei, Y. Ren, K.R. Asmis, S.-G. He, Catalytic Co-Conversion of CH₄ and CO₂ Mediated by Rhodium–Titanium Oxide Anions RhTiO²⁻, Angew. Chem. Int. Ed. 60 (2021) 13788–13792.